



Deposited via The University of Sheffield.

White Rose Research Online URL for this paper:

<https://eprints.whiterose.ac.uk/id/eprint/100803/>

Version: Accepted Version

Article:

Morton, R.J., Verth, G., Fedun, V. et al. (2013) Evidence for the photospheric excitation of incompressible chromospheric waves. *Astrophysical Journal*, 768 (1). ARTN 17. ISSN: 0004-637X

<https://doi.org/10.1088/0004-637X/768/1/17>

Reuse

Items deposited in White Rose Research Online are protected by copyright, with all rights reserved unless indicated otherwise. They may be downloaded and/or printed for private study, or other acts as permitted by national copyright laws. The publisher or other rights holders may allow further reproduction and re-use of the full text version. This is indicated by the licence information on the White Rose Research Online record for the item.

Takedown

If you consider content in White Rose Research Online to be in breach of UK law, please notify us by emailing eprints@whiterose.ac.uk including the URL of the record and the reason for the withdrawal request.

EVIDENCE FOR THE PHOTOSPHERIC EXCITATION OF INCOMPRESSIBLE CHROMOSPHERIC WAVES

R. J. MORTON^{1,2}, G. VERTH¹, V. FEDUN^{1,3}, S. SHELYAG^{4,5}, R. ERDÉLYI¹

¹Solar Physics and Space Plasma Research Centre (SP²RC), University of Sheffield, Hicks Building, Hounsfield Road, Sheffield S3 7RH, UK

²Mathematics and Information Sciences, Northumbria University, Newcastle Upon Tyne, NE1 8ST, UK

³Department of Automatic Control and Systems Engineering, University of Sheffield, Mappin Street, Sheffield, S1 3JD, UK

⁴Astrophysics Research Centre, School of Mathematics and Physics, Main Physics Building, Queen's University Belfast, Belfast, County Antrim, BT7 1NN, UK

⁵Monash Centre for Astrophysics and School of Mathematical Sciences, Monash University, Clayton, Victoria 3800, Australia

(Dated: Received /Accepted)
Draft version March 12, 2013

ABSTRACT

Observing the excitation mechanisms of incompressible transverse waves is vital for determining how energy propagates through the lower solar atmosphere. We aim to show the connection between convectively driven photospheric flows and incompressible chromospheric waves. The observations presented here show the propagation of incompressible motion through the quiet lower solar atmosphere, from the photosphere to the chromosphere. We determine photospheric flow vectors to search for signatures of vortex motion and compare results to photospheric flows present in convective simulations. Further, we search for the chromospheric response to vortex motions. Evidence is presented that suggests incompressible waves can be excited by the vortex motions of a strong magnetic flux concentration in the photosphere. A chromospheric counterpart to the photospheric vortex motion is also observed, presenting itself as a quasi-periodic torsional motion. Fine-scale, fibril structures that emanate from the chromospheric counterpart support transverse waves that are driven by the observed torsional motion. A new technique for obtaining details of transverse waves from time-distance diagrams is presented and the properties of transverse waves (e.g., amplitudes and periods) excited by the chromospheric torsional motion are measured.

Subject headings: Sun: Photosphere, Sun: Chromosphere, Waves, MHD

1. INTRODUCTION

Magnetohydrodynamic (MHD) wave phenomena have now been observed to be ubiquitous throughout the solar atmosphere and are considered to be a potential mechanism for the transport of energy for the heating of the solar atmosphere and the acceleration of the solar wind (for reviews, see, e.g., Aschwanden, 2005; Klimchuk, 2006; Erdélyi, 2006). However, no individual mechanism has yet been identified for converting a portion of the mechanical energy generated in the Sun's convection zone to heat.

Both incompressible and compressible MHD waves are widely reported throughout the solar atmosphere (for reviews, see, e.g., Banerjee et al., 2007, Zaqarashvili & Erdélyi, 2009, Wang, 2011, De Moortel & Nakariakov, 2012) and incompressible waves in the solar wind (e.g., Tu & Marsch, 1995). Recent advances in ground and space-based solar telescopes have allowed for the detection of ubiquitous incompressible transverse waves, both in the chromosphere (De Pontieu et al., 2007; He et al., 2009a,b; Okamoto & De Pontieu, 2011; Antolin & Verwichte, 2011; Kuridze et al., 2012; Morton et al., 2012) and in the solar corona (Tomczyk et al., 2007, Erdélyi & Taroyan, 2008). However, the incompressible waves are difficult to dissipate without strong gradients in Alfvén speed (e.g., resonant absorption - Ionson, 1978) or some process to cause a cascade of the wave energy to higher frequencies (e.g., MHD turbulence - Matthaeus et al., 1999) where they are efficiently dissipated by, e.g., cyclotron damping (McKenzie et al.,

1997).

The solar magnetic field acts as a channel with the potential to distribute wave energy around the solar atmosphere. In the quiet Sun at the photospheric level, a large percentage of the magnetic flux appears to be concentrated into intense magnetic elements (spatial scales of 100 – 200 km) that outline the supergranule network. Some of these concentrations of magnetic flux are observed to undergo a significant expansion at the chromosphere/Transition Region, forming magnetic funnels that could be preferential sites for solar wind acceleration or the legs of large-scale coronal loops (Peter, 2001). The remainder of the flux may form cell-spanning chromospheric structures, providing a magnetic canopy (Dowdy et al., 1986; Rutten, 2006, 2007; Wedemeyer-Böhm et al., 2009). Smaller concentrations of magnetic flux also exist in the internetwork (e.g., Faurobert et al., 2001; Domínguez Cerdeña et al., 2003; Schrijver & Title, 2003), potentially generating additional magnetic structure below the magnetic canopy.

The largest source of wave-energy is the continually evolving sub-photospheric convection, which generates a wide spectrum of MHD fluctuations. The influence of convection on the magnetic elements is well studied at the photospheric level. Typically, the observations have focused on tracing the motion of strong, localised magnetic flux elements, referred to as magnetic bright points (MBPs) when seen in the G-band 4305 Å line (e.g., Title et al., 1989, Berger et al., 1995, Berger et al., 1998, Berger & Title, 2001, Sánchez Almeida et al., 2004) or more recently in the H α line wings (Leenaarts et al., 2006, Chitta et al., 2012). The continuous jostling of the MBPs leads to

the excitation of MHD waves and oscillations, well described by the theory of MHD oscillations in magnetic flux tubes (e.g., Spruit, 1982; Edwin & Roberts, 1983; Erdélyi & Morton, 2009; Erdélyi & Fedun, 2010).

One particular aspect of convective motion that has received increased attention recently is the generation of vortices at the solar surface. Observations (Brandt et al., 1988; Bonet et al., 2008; Balmaceda et al., 2010) and advanced simulations (Moll et al., 2011; Shelyag et al., 2011b) of solar granulation have revealed these vortex features are almost everywhere on the solar disk. Wedemeyer-Böhm & Rouppe van der Voort (2009) and Wedemeyer-Böhm et al. (2012) have demonstrated that the vortex motion has an observable influence on the upper layers of the solar atmosphere, suggesting they may play a role in heating. Further, simulations of Fedun et al. (2011b) have demonstrated that the twisting of an open flux-tube by vortices at the photospheric level leads to the generation of MHD waves, in particular incompressible (i.e., torsional Alfvén and transverse/kink) waves.

The transverse waves have recently been the subject of some controversy, with discussions on their nature, properties and nomenclature. The properties of the transverse waves in solar magnetic flux tubes are well understood (e.g., Edwin & Roberts, 1982; Spruit, 1982; Edwin & Roberts, 1983; Erdélyi & Fedun, 2007), with a significant volume of research dedicated to developing realistic models, including, e.g., magnetic structuring (Verth & Erdélyi, 2008; Ruderman et al., 2008), density structuring (Andries et al., 2005; Dymova & Ruderman, 2005), flux tube geometry (Van Doorsselaere et al., 2004; Dymova & Ruderman, 2006; Erdélyi & Morton, 2009; Morton & Erdélyi, 2009), multiple flux tubes (Robertson et al., 2010; Luna et al., 2010; Pascoe et al., 2011), resonant damping (Ruderman & Roberts, 2002; Goossens et al., 2002; Terradas et al., 2006; Terradas et al., 2010), partial ionization (Soler et al., 2009a,b; Zaqrashvili et al., 2011).

One of the most important properties of the low-frequency transverse waves is that they are highly incompressible (Goossens et al., 2009), requiring large gradients in the Alfvén speed to damp the waves. It is this property (shared with low-frequency bulk Alfvén waves of a homogeneous plasma) that means incompressible waves can pass through the lower solar atmosphere relatively undamped, making them a good candidate for acceleration of the solar wind. Observations of incompressible waves in the quiet chromosphere (De Pontieu et al., 2007; Morton et al., 2012), quiet corona (Tomczyk et al., 2007; Erdélyi & Taroyan, 2008) and the solar wind (Tu & Marsch, 1995) support this idea. Another important property, that makes these waves relatively easy to observe, is that the transverse wave causes a physical displacement of the flux tubes axis.

To assess exactly what role the incompressible MHD waves play in determining the dynamics of the solar atmosphere, one needs to combine advance models of wave propagation throughout the atmosphere (e.g., Cranmer & van Ballegoijen, 2005; Cranmer et al., 2007; Matsumoto & Shibata, 2010; Antolin & Shibata, 2010; Fedun et al., 2011a, van Ballegoijen et al., 2011, Vigeesh et al., 2012) with

observations. The observations should aim to determine how the waves are being generated and track the wave-energy as it propagates through the solar atmosphere. This should reveal how much wave energy is present in each distinct region of the solar atmosphere and where the dissipation of this energy occurs. The tracking of waves through the solar atmosphere has been made a realistic possibility by the development of high spatial and temporal resolution multi-filter systems, that can observe different heights in the lower atmosphere simultaneously (e.g., Rapid Oscillations in the Solar Atmosphere (ROSA), CRisp Imaging Spectro-Polarimeter). The potential of these observational set-ups for wave tracking is demonstrated in Vecchio et al. (2007), Jess et al. (2012a,b). Such ground-based telescopes complement the satellites, e.g. Hinode, Solar Dynamics Observatory (SDO), which provide detailed observations in UV/EUV.

This paper reports the observation of both chromospheric torsional Alfvén and kink waves and provides evidence that the waves are generated by photospheric vortices. The analysed data is a high resolution, high cadence series of G-band, Calcium K and Hydrogen α lines observed with ROSA located at the Dunn Solar Telescope, USA. The ROSA observations are supplemented with SDO data. Photospheric flows are determined using Local Correlation Tracking (LCT) and compared to numerical simulations of convection (Section 4). A statistical method for obtaining information on chromospheric kink waves is described based on the analysis of time-distance diagrams.

2. OBSERVATIONS AND DATA REDUCTION

The data presented here has been studied in part in Kuridze et al. (2012) and Morton et al. (2012). The data were obtained at 15:41-16:51 UT on 29 September 2010, with the Dunn Solar Telescope at Sacramento Peak, USA. A six-camera system called ROSA was employed, details of which are given in Jess et al. (2010). In brief, a $69''.3 \times 69''.1$ region of the quiet solar atmosphere, positioned close to disk centre (N0.9, W6.8), was imaged with a spatial sampling of $0''.069 \text{ pixel}^{-1}$. We note here this is the corrected pointing to that given in Kuridze et al., 2012.

During the observations, high-order adaptive optics (Rimmele, 2004) were used to correct for wave-front deformations in real time. The seeing conditions were good but variable. Some frames in each of the data series are subject to significant distortions. We exclude periods of seeing containing frames of inadequate quality.

ROSA obtained images in multiple wavelengths including G-band (4305.5 Å- 9 Å width), Ca K (3933.7 Å) narrowband (1 Å) and H α core (6562.8 Å) narrowband (0.25 Å) filters. The G-band data was sampled at 16.6 frame s^{-1} , H α at 2.075 frame s^{-1} and Ca K 1.66 frame s^{-1} and the images were improved by using speckle reconstruction (Wöger et al., 2008) utilising a 16 – 1 ratio. The cadence of the reconstructed G-band, H α and Ca K time-series are 0.96 s, 7.7 s and 9.6 s, respectively. To ensure accurate co-alignment in all bandpasses, the broadband times series were Fourier co-registered and de-stretched (Jess et al., 2007).

Images from the SDO Atmospheric Imaging Assembly (AIA) are also presented to provide context for the

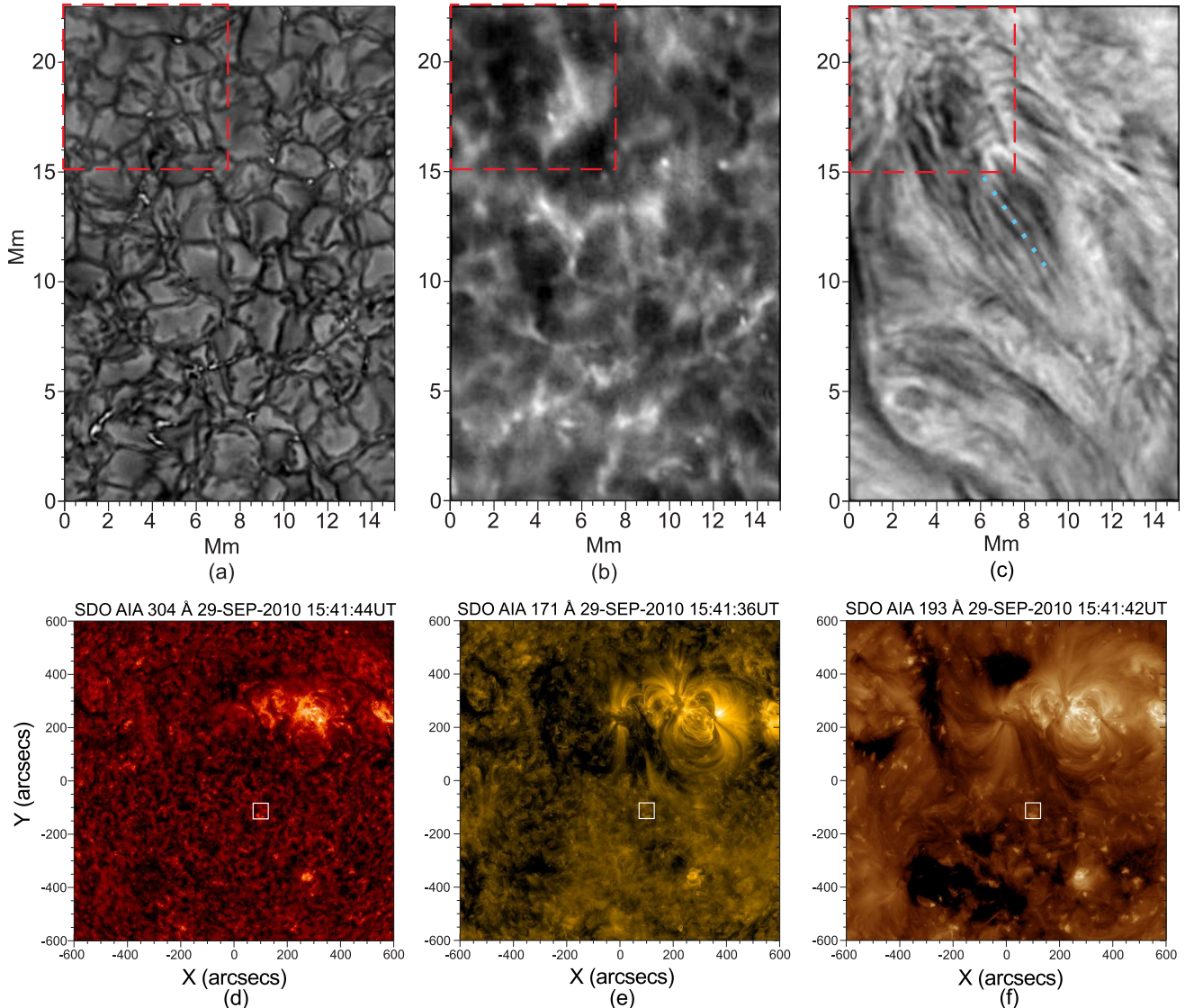


FIG. 1.— A region of the quiet solar atmosphere as observed by ROSA. (a) G-band image showing a 15 by 23 Mm² sub-region of the ROSA field of view. Collections of magnetic bright points are clearly visible in the inter-granule lanes. (b) Ca K image of the lower chromosphere. (c) H α core image of the mid to upper chromosphere. The existence of fine-scale structuring in the bandpass is evident, with both spicules/mottles and cell-spanning fibrils identifiable. The blue dots show the path along which perpendicular cross-cuts were taken, see Section 5 for further details. The bottom row displays images of the upper solar atmosphere observed by SDO/AIA. The panels show (d) 304 Å, (e) 171 Å and (f) 193 Å filters. The axis show solar coordinates. The white boxes highlight the region which ROSA observed.

state of the upper atmosphere above the above the ROSA field of view. The images from SDO are processed with *aia_prep* and have a spatial resolution of $0''.6 \text{ pixel}^{-1}$.

3. THE MAGNETIC STRUCTURE

The region of the Sun observed by ROSA is a typical quiet Sun area. The focus of the investigation will be on a sub-region of the ROSA field of view that contains a feature of particular interest. Images of this sub-region are shown in Fig. 1. In the G-band images, a number of MBPs are clearly identifiable. The bright points are a good proxy for strong concentrations of magnetic flux, however, strong magnetic flux can still be present without an associated MBP (Berger & Title, 2001). Specific conditions appear to be needed for an MBP to appear in G-band (e.g., Carlsson et al., 2004; Ishikawa et al.,

2007). On viewing the movie of the G-band time series, the MBPs are seen to be pushed and jostled by the convective motions of the granules, merging and splitting and appearing and disappearing from the bandpass.

The Ca K images (Fig. 1b) also show bright points, displaying a close mapping to the MBP's seen in G-band. This suggests the Ca K bright points are the chromospheric counterpart to the G-band MBPs. However, the Ca K bright points are more diffuse, possibly due to expansion of the magnetic flux with height and partially due to the properties of the filter. The bright points are also more persistent than the G-band MBPs, hence show a different morphology. The images also contain acoustic grains and reversed granulation, which have been identified previously. These features (possibly including the diffuse MBP nature) are present due to the large width of

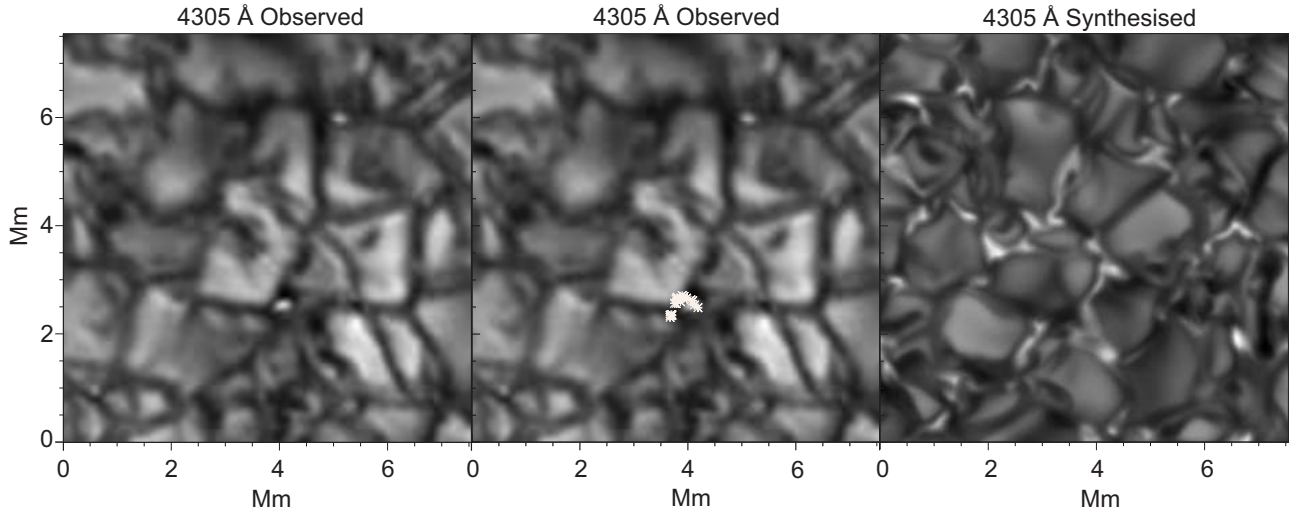


FIG. 2.— The *left* panel displays the G-band region enclosed in the red box in Fig. 1. The motion of an MBP flows derived with a point and click method is highlighted by the over-plotted stars (*middle panel*). The motion is from left to right. The *right* image is the synthesised G-band from the MURaM code.

the filter bandpass used for these observations, meaning that the Ca K images here have contributions from both photospheric and chromospheric sources (for a detailed explanation, see Leenaarts et al., 2006). Selecting a sufficiently narrow filter to image Ca K line centre can avoid the photospheric contamination and allow mainly chromospheric contributions (see, e.g., Cauzzi et al., 2008; Reardon et al., 2009; Pietarila et al., 2009).

In the $H\alpha$ core bandpass (Fig. 1c), few signatures of the MBPs are visible. The region is covered with fine-scale structure, such as elongated, cell-spanning fibrils and a few shorter mottles (jet-like structures). Due to the narrow width of the filter, the $H\alpha$ core images show the ‘true’, magnetically dominated (low- β) chromosphere (Rutten, 2006, 2007). The observed features, i.e., the fibrils and mottles, are thought to highlight the chromospheric magnetic field, with the structures likely to be density enhancements along individual magnetic field lines (this is supported by recent modelling of $H\alpha$ line formation by Leenaarts et al., 2012).

In the following section we pay particular attention to the area highlighted by the dashed box in Fig. 1. A number of fibrils and mottles can be seen to emanate from this region. At the photospheric level, the G-band images reveal that a number of MBPs appear and disappear. The counterpart Ca K bright points remain present, although some of the brighter elements fade and brighten with time. These underlying features lead us to suggest the highlighted $H\alpha$ region is the chromospheric section of a of a magnetic flux concentration, associated with an MBP, that has undergone significant expansion from the photosphere. The observed MBPs diameters are $\sim 100 - 200$ km while the $H\alpha$ feature has a diameter of ~ 3000 km. The described magnetic structure is thought to be common in the quiet solar atmosphere (e.g., Dowdy et al., 1986; Peter, 2001) and is also revealed in observations of chromospheric swirls by Wedemeyer-Böhm & Rouppe van der Voort (2009) and Wedemeyer-Böhm et al. (2012).

The magnetic structure above the chromosphere is much harder to determine. Fig. 1 (d-f) displays images

from SDO/AIA in the 304 \AA , 171 \AA and 193 \AA band-passes. A near-by active region is visible in the upper right hand corner of each image, however, it can be seen that the ROSA field of view is far from the active region in an area of quiet Sun.

4. FLUX TUBE DYNAMICS

Now, our attention is focused on the dynamical behaviour of the unique region identified in the previous section (dashed box Fig. 1). To provide insight into the horizontal motions of the magnetic elements we exploit LCT. This technique was originally introduced into solar physics to track large-scale (spatial and temporal) photospheric flows, e.g., November & Simon (1988), and the technique has been developed further for use on magnetograms by incorporating the induction equation (e.g., DAVE - Schuck, 2006).

We developed an LCT algorithm based on the routine *tr_get_disp.pro* (developed by T. Tarbell) available in the SSW TRACE software tree. A recent version of this routine first apodizes a set of images using a Hanning function, then computes the cross-correlation between the images. The position of the maximum of the cross-correlation corresponds to the integer pixel shifts between the images. A local region centred on the maximum is then fitted with a quadratic polynomial regression equation to locate the maximum with sub-pixel accuracy, hence providing sub-pixel accuracy on the shifts.

The routine was tested on sample data, which consists of hundreds of different images taken from the ROSA data series. The images were shifted using the routine *shift_image.pro* (available in the general SSW software tree). Taking averages over large numbers of images, we find that shifts as small as 0.03 pixels can be resolved to within ± 0.005 pixels. The accuracy of the LCT improves with increasing shift size. There appears to be potential for great accuracy when calculating small shift values statistically, however, a more rigorous test of *tr_get_disp's* ability to resolve shifts is needed.

From the derived shifts we are able to determine the horizontal photospheric flow, U_h . Further, we can cal-

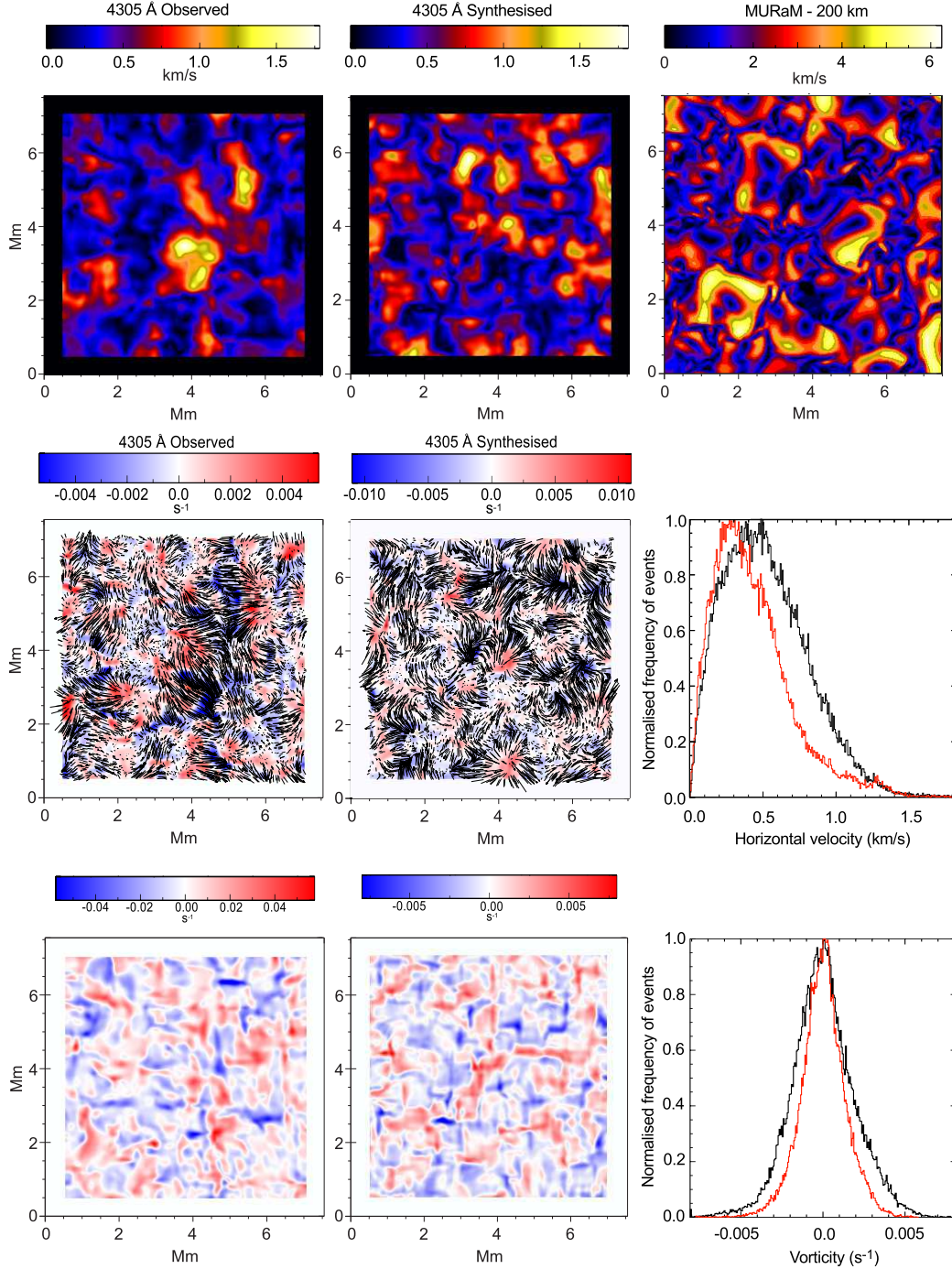


FIG. 3.— The top row shows the magnitudes of velocities of photospheric flows as determined from the observed G- band (*left*), the synthesised G-band (*middle*) and the MURaM code at a geometric height of 200 km above the continuum formation level (*right*). The velocities are averaged over 30 frames (~ 230 s). The *middle* row displays velocity vectors and divergence of photospheric flows. The arrows display the averaged velocity vectors determined with LCT from the observed (*left*) and simulated (*middle*) G-band. A histogram (*right*) showing the distribution of the horizontal velocity for the observed (red) and the simulated (black) data. The *bottom* row displays vorticity (s^{-1}) calculated from the horizontal photospheric flows. The panels displays the averaged vorticity from the observed (*left*) and simulated (*middle*) G-band. A histogram (*right*) showing the distribution of the vorticity for the observed (red) and the simulated (black) data.

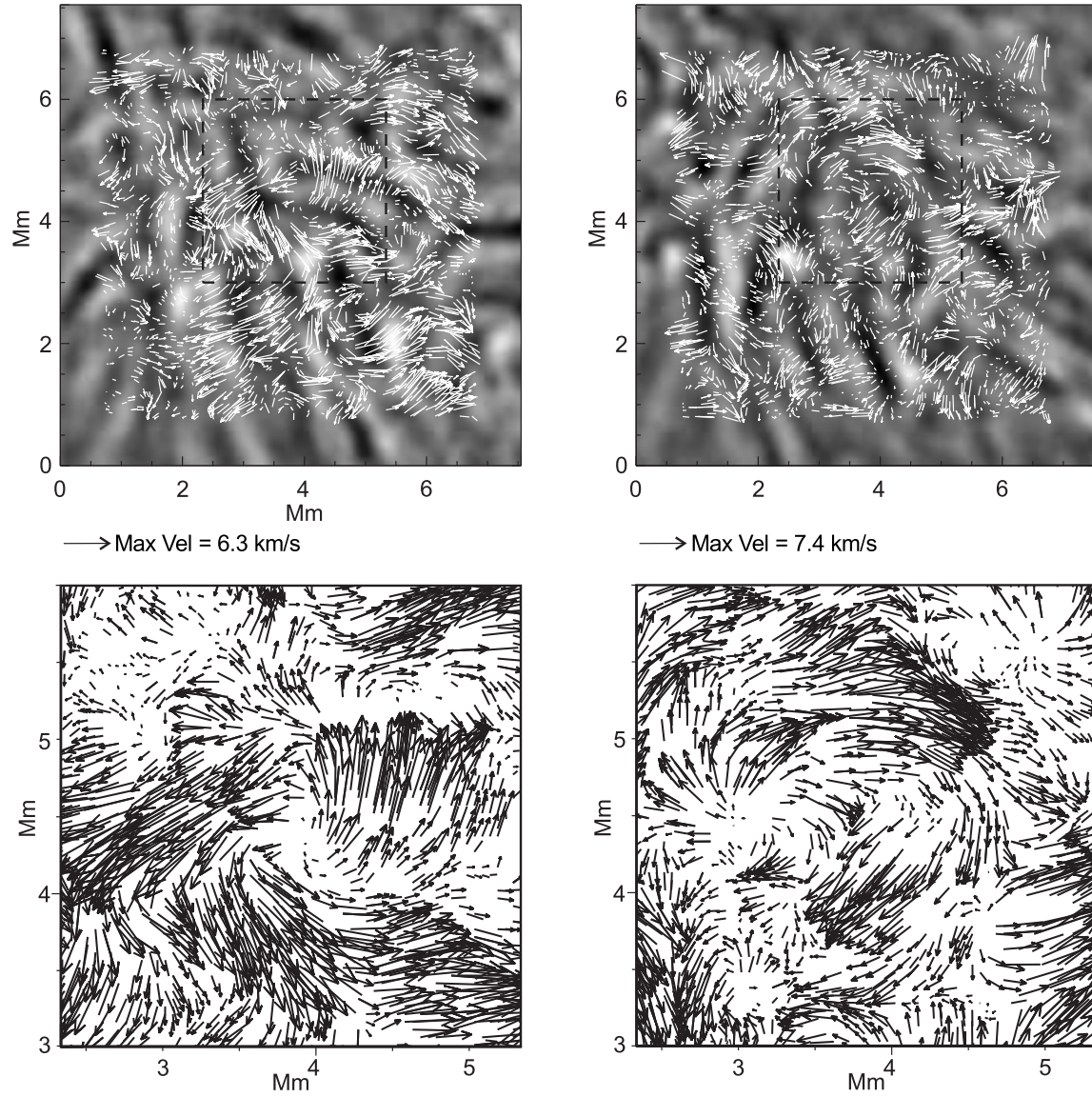


FIG. 4.— The chromospheric response to photospheric vortices. Torsional motion is observed in $H\alpha$ and demonstrated by applying LCT to frames between $t = 207 - 277$ s (left) and $t = 610 - 690$ s (right). The torsional motion is centred approximately on the point located at $(3.8, 4.5)$ Mm. The vectors are over plotted on the unsharp masked and atrous filtered $H\alpha$ data at $t = 200$ s (left) and $t = 600$ s (right). The region shown corresponds to the dashed box in Fig. 1c. The bottom row displays enlarged versions of the regions centred on $(3.8, 4.5)$ Mm (as marked by the boxes). The density of vectors has also been increased by a factor of two and a half.

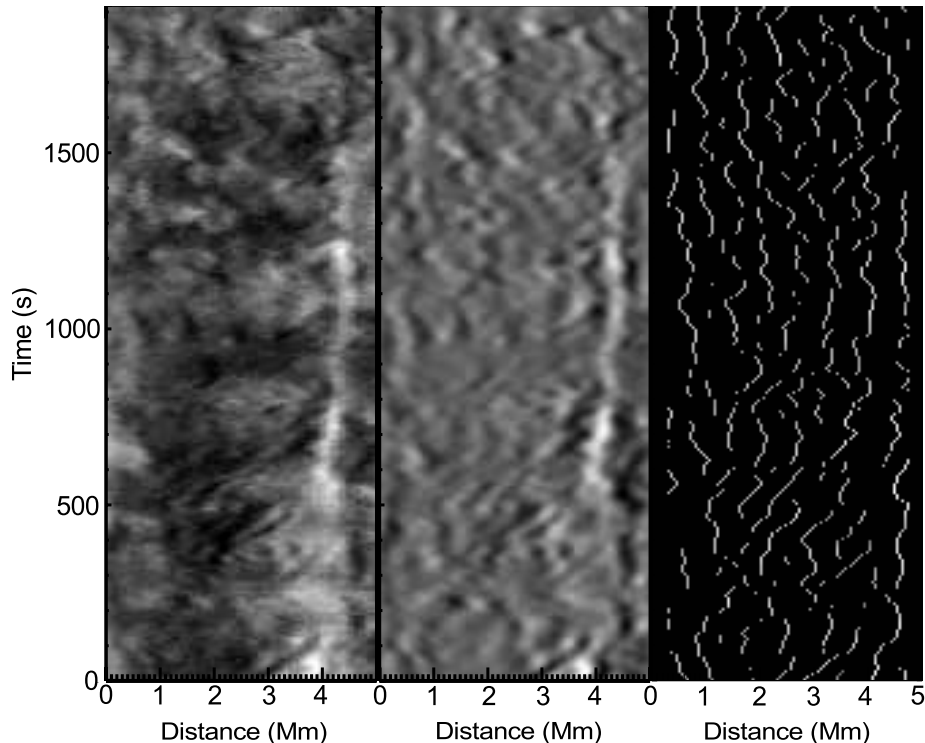


FIG. 5.— Overview of the technique for identifying transverse waves. The *left* panel shows time-distance plot of a cross-cut taken perpendicular to the fibrils (i.e., perpendicular to the dotted blue line in Fig. 1c). The *middle* panel is the same cross-cut that has been subject to unsharp mask and with the high frequency component removed. The *right* panel displays the fibril paths obtained from the time-distance plot in the middle panel. The lines highlight the dark features.

culate the divergence of the velocity, $\nabla \cdot U_h$, and the photospheric vorticity, $\nabla \times U_h$.

4.1. LCT on G-band data

The G-band data series has a very high cadence at 0.96 s. However, the previously reported values for photospheric flows are $1 - 2 \text{ km s}^{-1}$, hence the expected shift between each frame is < 0.03 pixels. To improve accuracy, every eighth frame is then selected from the G-band series, increasing the cadence to 7.68 s and expected shifts to > 0.08 pixels (0.5 km s^{-1}). Further, a sonic filter is applied to the data to suppress the influence of p-modes and stochastic variations in intensity. The data is then re-sampled using linear interpolation to achieve a pixel size of $25 \times 25 \text{ km}^2$.

The LCT is performed on frames chosen from the first sixty frames because the seeing during this period is relatively stable. For each data set that we apply LCT to, the LCT is performed on many sub-regions of the overall image, with window sizes determined by the dominant features at that wavelength. A window size of $40 \times 40 \text{ pixel}^2$ ($1 \times 1 \text{ Mm}^2$) is used such that features on the order of the granulation will contribute to the cross-correlation. This, along with the apodization of the window, will reduce the effect of large intensity gradients on resolving shifts.

The $7.5 \times 7.5 \text{ Mm}^2$ boxed region in Fig. 1a is selected (close-up of this region is shown in Fig. 2 left panel) and subject to the LCT algorithm. The photospheric flow is calculated over a 30 frame average, revealing long-lived flow patterns.

The magnitude of the photospheric velocities are shown in Fig. 3. A histogram plot of the velocity distri-

bution (Fig. 3) is in line with results from MBP tracking, e.g., Keys et al. (2011); Chitta et al. (2012), and from long-term flow measurements, e.g., November & Simon (1988), Berger et al. (1998). The velocity vectors and divergence are also shown in Fig. 3. The directions of the velocity vectors results are consistent with the flow direction as seen by a visual inspection of the G-band movie. Evidence for vortices are present, with the velocity vectors marking out curved paths or arcs thought to be demonstrating the vortex behaviour. This is verified by calculating the vorticity from the horizontal velocity, which demonstrates that vorticity is present across the the photospheric region (Fig. 3 - bottom row, left panel). A histogram of vorticity values is given in Fig. 3 and the values obtained here are in agreement with previous observational measurements (e.g., Brandt et al., 1988; Vargas Domínguez et al., 2011).

In addition, the motion of an individual MBP is tracked over twenty frames using a crude (but efficient) point and click method. The MBP selected lies directly under the chromospheric feature, which suggests it is the photospheric counterpart. The tracking of the individual bright point reveals the MBP follows an arc-shaped path across the photosphere, demonstrating the MBP is in the presence of a photospheric vortex. This is confirmed as the MBP is also seen to lie in a region of strong, negative vorticity in Fig. 3.

4.2. LCT on simulated G-band data

To validate the results of the LCT technique, we performed tests on a numerically simulated G-band image sequence. The synthetic data were produced using radiative diagnostics of the three-dimensional numerical

model of magnetised lower solar atmosphere (i.e. convection zone and photosphere) generated by MURaM radiative MHD code (Vögler et al., 2005). The domain size chosen is $12 \times 12 \times 1.4 \text{ Mm}^3$ in the horizontal and vertical directions respectively, and the horizontal resolution is 25 km. The detailed G -band radiative diagnostics was carried out using the radiative transport code, designed for computationally efficient wide band filter calculations (see, Jess et al., 2012b for more details). We have generated 800 G -band images of solar granulation with the average vertical magnetic flux of 200 G (the value of magnetic field strength is consistent with recent observations, e.g., Orozco Suárez & Bellot Rubio, 2012). The time cadence for the image sequence is about 2 seconds and not constant due to variation of the time step in the numerical simulation.

To provide a direct comparison with the observational analysis described in the previous section, the resolution of the simulated data is reduced to 50 km, using every fourth frame to achieve a similar cadence. We apply the sonic filter and re-sample using linear interpolation to 25 km. The LCT results are averaged, again, over 30 frames. The results of LCT on the simulated G -band image sequence demonstrate qualitatively similar plasma flow patterns in both the granular and intergranular regions to the observed data (Fig. 3). The results from the simulated data show slightly greater values of divergence and vorticity. The absolute values of velocity and vorticity in the simulated data are plotted in a histogram (Fig. 3) for direct comparison between the observed and synthesised G -band images. The distributions can be seen to be comparable although slight differences exist between the observed and simulated values. This can be attributed to the fact that the observed and simulated regions are inherently different regions, with an unknown quantity of magnetic flux in the observed region. Some of the differences may also lie in the quality of the observed data. A measure of the difference in quality is the root mean squared contrast. The synthesised G -band images have a mean RMS of 0.17 ± 0.003 , while the observed G -band images have a much lower mean RMS of 0.11 ± 0.02 and much greater variation in RMS between frames.

The flow speeds in the simulations have also been measured at the geometrical height of approximately 200 km above the continuum formation level. They show the presence of the flow features similar to those detected by LCT applied to the simulated G -band images (Fig. 3). However, due to measurement of the flow speeds at the constant geometrical height instead of at optical depth corresponding to the G -band radiation formation, only a qualitative comparison of these speeds with the speeds obtained by LCT is valid and possible.

The simulations are known to be replete with vortex motions. The agreement seen between LCT results performed on the observed and simulated data gives us confidence that the photosphere also contains numerous vortex structures. Torsional Alfvén waves have been shown to be excited at the photospheric level in a number of numerical simulations. They are excited in magnetic photospheric vortex structures by random motions, such as granular flows (see, for example, numerical simulations of photospheric magneto-convection, e.g. van Ballegoijen et al., 2011; Kitiashvili et al., 2011;

Shelyag et al., 2011a, Shelyag et al., 2012a,b; Moll et al., 2012), and by synthetic photospheric torsional (vortex-type) drivers (e.g., Fedun et al., 2011a,c, Vigeesh et al., 2012) in the idealised simulations of solar magnetic flux tubes.

We note the magnetic vortex structures significantly differ in their nature and dynamics from the non-magnetic vortices (see, e.g., Stein & Nordlund, 1998, Kitiashvili et al., 2012). They, and the torsional Alfvén waves they produce, generate large amounts of Poynting flux (see, e.g., Fedun et al., 2011b, Shelyag et al., 2012a,b). As has been shown by Wedemeyer-Böhm et al. (2012), the magnetic vortex structures expand from the photospheric level into the corona. They are suggested channels for electromagnetic energy to tunnel into the higher layers of the solar atmosphere and, therefore, such structures are considered as potential channels of energy transport for coronal heating.

4.3. LCT on $H\alpha$ data

On inspecting the $H\alpha$ movie, a torsional (or rotational) motion is observable in the area highlighted with the dashed box in Fig. 1c. A chromospheric response to photospheric vortices has already been observed in high-resolution observations of the lower chromosphere (Wedemeyer-Böhm & Ruppe van der Voort, 2009, Wedemeyer-Böhm et al., 2012). So far, the reported chromospheric swirl events appear to demonstrate rotation in *one* direction only. Here, the $H\alpha$ region appears to first rotate in one direction and then rotate in opposite direction quasi-periodically. Such behaviour has been observed in the intergranular vortices in realistic simulations of magneto-convection Shelyag et al. (2012a, 2011b), as well as in the idealised simulations of flux tubes in the quiet Sun (Fedun et al., 2011c). This would suggest the presence of torsional Alfvén waves, which have also been identified previously in chromospheric features situated above MBPs (Jess et al., 2009).

To demonstrate this behaviour, LCT is applied to the $H\alpha$ data. Before performing LCT, the unsharp-mask (USM) technique is applied to the full field of view and the mask is subtracted. The mask is created using a box-car average of width 20 pixels. This technique has two benefits: (i) the removal of large spatial-scale intensity perturbations which could influence results; (ii) an increased contrast between chromospheric features and the background. The intensity perturbations (Morton et al., 2012) are removed from the time series because they are coherent over a large spatial-scale. Further, an atrous spatial filtering algorithm (e.g., Starck & Murtagh, 2002) is applied to each frame. The highest frequency component from the spatial filtering contains mainly noise, which is then subtracted to improve the signal to noise in each image.

The torsional motion appears quasi-periodic with an apparent period between 120-180s, hence, the LCT is averaged over sets of 9 consecutive frames. Note, the period range given is based on the apparent rate at which the motion appears to change its direction of rotation. The time-series shows the rotation change directions a number of times over its duration. This is calculated by eye from viewing the $H\alpha$ time-series and we do not consider it a rigorous measurement of the period. The velocity vector plots in Fig. 4 confirm the visual impres-

sion of torsional motion. The first vector plot is averaged over the frames in the range 207 – 277 s and the second vector plot is averaged over 610 – 690 s. These time ranges are used as they correspond to the times when the torsional motion is most evident. The torsional motion is centred on the region around (3.8, 4.5) Mm in the plots and a zoom of this region (Fig. 4 - bottom row) reveals the signature of the torsional motion. The maximum values of the velocity amplitude of the torsional motion are $\sim 7 \text{ km s}^{-1}$ with an average and standard deviation of $1.8 \pm 1.4 \text{ km s}^{-1}$. These values are essentially the time-averaged velocity amplitudes, while the peak amplitudes are likely greater as the peak value is a factor of $\sqrt{2}$ greater than the time-averaged amplitude.

5. TRANSVERSE WAVES

The focus of this work is now shifted to the fine-scale structure that originates in the previously identified H α region. The fine-scale structure we are interested in are the dark, absorption features, which are mainly elongated, inclined fibrils and a few mottles (nearly vertical structures thought to be similar to spicules). On inspecting the movie of H α , the fine-scale structure can be identified to exhibit transverse motion. The fibrils are rooted in the region where the torsional motion is observed and the torsional motion shakes the fibrils footpoints side to side, which drives the transverse waves. In this section we study the transverse waves supported by these structures and demonstrate new techniques for obtaining information about the waves.

To model these transverse waves, the assumption is made that the waves are propagating along an overdense, magnetic flux tube embedded in an ambient plasma environment. The speed at which these waves propagate is known as the kink speed, which is defined as,

$$c_k = \sqrt{\frac{\rho_i v_{Ai}^2 + \rho_e v_{Ae}^2}{\rho_i + \rho_e}}. \quad (1)$$

where ρ is the density and $v_A = B^2/(\rho\mu_0)$ is the Alfvén speed, B is the magnetic field and μ_0 is the magnetic permeability. Here, we follow convention labelling internal and ambient plasma parameters with subscripts i and e , respectively.

The first step in the analysis of the observed transverse waves is to apply the USM procedure to the H α images. The orientation of the fine-scale structure is determined (see dotted line over plotted on the H α image, Fig. 1c) and a series of 42 cross-cuts, separated by 2 pixels, are placed perpendicular to their axis. From the cross-cuts, time-distance plots are created, an example of which is shown in Fig. 5. The time-distance plots clearly reveal the transverse motions of the fibril structures. Next, to reduce the background noise, an atrous filtering algorithm is applied to the time-distance plots and the highest frequency component is subtracted.

The individual, dark fibrils in each cross-cut are then located in the following manner. Cross-sectional flux profiles of fibrils have an almost Gaussian shape, with the minimum value of intensity at the centre of the fibril cross-section. For each time slice, the pixels with the minimum intensity in a localised region are located. A gradient threshold is then applied allowing for isolated

fibrils to be located. The gradient of the neighbouring 5 points on either side of the minimum value pixel is calculated and has to be larger than the threshold value for the minimum point to be selected. Should two fibrils approach each other or begin to cross, the gradient becomes shallower around the minima. Optimisation of the threshold level allows for a significant number of isolated fibrils to be identified (Fig. 5c), with the fibril paths in time being traced out. This method only locates the centre of the structure to within one pixel and hence has an error of $\pm 50 \text{ km}$ on each point.

For each fibril path identified at this stage, we then select only the paths that obey certain conditions: (i) the path has to be longer than 5 pixels; (ii) The maximum time separation between neighbouring points in the thread has to be less than 4 pixels (30 s), the ‘missing’ pixels are then recorded as having the same spatial position as that of the first of the time-separated neighbours; (iii) Points neighbouring in time cannot be separated spatially by more than 4 pixels (200 km). This last condition would limit any measured velocity amplitudes to $< 26 \text{ km s}^{-1}$.

Once we have selected the fibril paths, the results are then fitted with a Levenberg-Marquardt non-linear fitting algorithm (mpfit.pro - Markwardt, 2009). A function of the form

$$F(t) = G(t) + A \sin(\omega t - \phi) \quad (2)$$

is used to fit the oscillations. Here, $G(t)$ is a linear function, A is the displacement amplitude of the oscillation, ω the frequency and ϕ the phase of the oscillation. The fitting algorithm is supplied with the errors on each data point, where it is assumed the given error is the one- σ uncertainty. The fitting routine also calculates the one- σ error to each fit parameter. The fitted results are kept if the threads are longer than $3 \cdot 2\pi/4\omega$ and the errors on the fitted parameters are smaller than the magnitude of the parameter values. Transverse velocity amplitudes for the waves can be obtained from the fit using the relation $v_{\perp} = \omega A$ and errors in the velocity amplitude are calculated by summing in quadrature.

Over the 42 cross-cuts a total of 1100 oscillations are measured. A histogram of the periods, transverse amplitudes and velocity amplitudes are given in Fig. 6. A Gaussian fit to the distributions gives means and standard deviations of $P = 94 \pm 61 \text{ s}$, $A = 71 \pm 37 \text{ km}$ and $v_{\perp} = 4.5 \pm 1.8 \text{ km s}^{-1}$. It is also interesting to plot period versus displacement amplitude (Fig. 6 - bottom row left panel). It is apparent that there is a direct relationship between transverse displacement amplitude and period. We perform a weighted linear fit to the data points, calculated with the Levenberg-Marquardt algorithm with the constraint the line passes through (0,0). The result is over-plotted and the derived velocity amplitude from the trend is $\sim 4.2 \text{ km s}^{-1}$, in agreement with the mean value.

In Fig. 6 (bottom row right panel) the velocity amplitude as a function of period is shown. Qualitatively the velocity amplitude appears relatively constant as a function of period, however, a weighted linear fit to the data points suggest the velocity amplitude decreases with period. This implies that the energy, which is proportional to the square of the velocity, contained within this frequency range of waves (2-30 mHz) is approximately con-

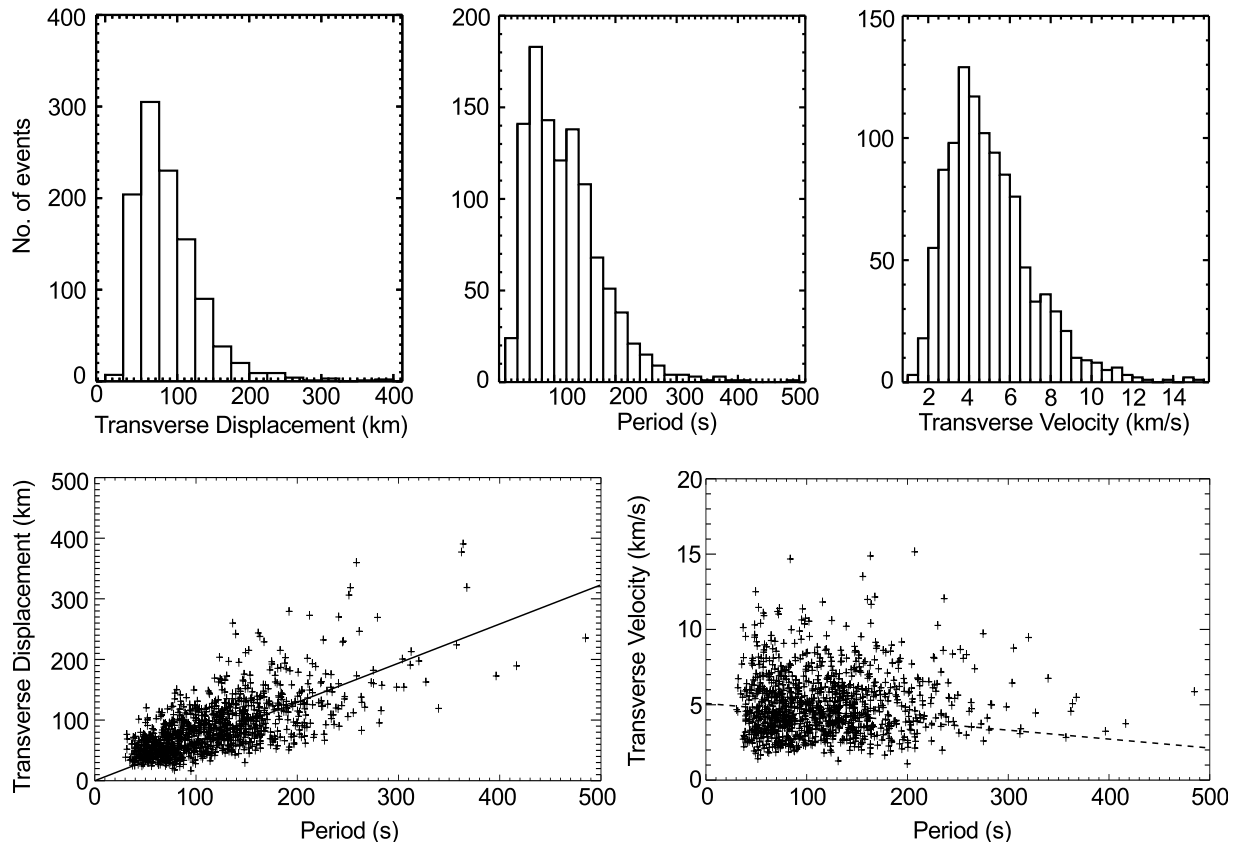


FIG. 6.— Histograms of measured properties of transverse motions for chromospheric fine structure originating in the region displaying torsional motion (*top row*). The histograms show, from left to right, the period, transverse displacement amplitude and transverse velocity amplitude. The mean and standard deviations are $P = 94 \pm 61$ s, $A = 71 \pm 37$ km and $v_{\perp} = 4.5 \pm 1.8$ km s $^{-1}$. Measured properties of the transverse waves (*bottom row*). (*left*) Period versus displacement amplitude. The solid line is a weighted fit to data points that gives a velocity amplitude of ~ 4.5 km s $^{-1}$. (*right*) Period versus velocity amplitude. The dashed line is weighted linear fit to the data points.

stant as a function of period. It is worth noting that the estimates of the temporal power spectra of the horizontal velocity of the photosphere by Matsumoto & Kitai (2010) using the G-band filter of *Hinode/SOT* showed a change of trend in the log-log gradients of Fourier power vs frequency at 4.7 mHz (approximately 213 s period). For frequencies less than 4.7 mHz they found an $f^{-0.6}$ relationship and for frequencies greater than 4.7 mHz it was $f^{-2.4}$. The derived photospheric power spectra, found by the method of LCT were taken as a proxy for the actual photospheric driver of transverse waves for a numerical simulation by Matsumoto & Shibata (2010) (in their case the $m = 0$ torsional Alfvén wave and not the $m = 1$ kink waves we observe here). A number of questions now arise, in comparing our measurements of transverse chromospheric velocity amplitude vs period measurements in chromospheric fibrils with the photospheric power spectra of Matsumoto & Kitai (2010). Firstly, our results suggest that Matsumoto & Shibata (2010) may have used the incorrect input power spectra, i.e., we see no evidence of wave energy decreasing with decrease in period. This is particularly relevant for wave heating since, mechanisms such as resonant absorption, phase mixing and ion-neutral damping are all more efficient at higher frequencies. On the other hand, if the photospheric power spectra obtained by Matsumoto & Kitai (2010) are a reasonable proxy for the driver of transverse waves, the output is notably different at chromospheric

heights and must be explained by further study.

We should note that all fits calculated here are under the assumption that the error in the period can be neglected over the error in the transverse displacement and velocity amplitudes. This may be justified as the mean error on the period, transverse displacement and velocity amplitudes are 8%, 21% and 23%, respectively.

6. DISCUSSION AND CONCLUSIONS

Tracking wave propagation through the lower layers of the solar atmosphere is an important step in being able to assess the viability of the various suggested mechanisms for atmospheric heating and solar wind acceleration. In Section. 4 we present observational evidence that photospheric vortices occur in the regions of strong magnetic flux concentrations. This is found to be in good agreement with the predictions of advanced models of solar magnet-convection. Further, we provide evidence that demonstrates the photospheric vortices can excite torsional motions in the chromosphere. This is supported by previous results from various numerical simulations (e.g., van Ballegoijen et al., 2011; Kitiashvili et al., 2011; Shelyag et al., 2011a, 2012a,b, Fedun et al., 2011a,c, Moll et al., 2012, Vigeesh et al., 2012) and previous observations (e.g., Wedemeyer-Böhm et al., 2012). The observation of the vortex and torsional motions is achieved by exploiting LCT to track the motions of both photospheric and chromospheric fea-

tures and identifying the signatures in the resulting velocity vector plots. The chromospheric torsional motion appears periodic here (unlike the unidirectional motion identified in swirl events, e.g., Wedemeyer-Böhm & Rouppe van der Voort, 2009), although we cannot resolve the periodic behaviour explicitly. The vector plots demonstrate that the region rotates one way and, at a later time, in the opposite direction. A better way to obtain details on torsional waves may be to exploit spectroscopic observations (e.g., Jess et al., 2009).

Further, the torsional motion is observed to excite transverse waves in the chromospheric fine-structure whose footpoints are rooted in the region. The fine-structure takes the form of elongated absorption features that are fibrils and a few shorter features, possibly mottles. The transverse velocity amplitudes of the transverse waves are comparable to the velocity amplitudes obtained from averaging of the torsional motion. The observations imply that the transverse waves are driven by the torsional motion, which in turn is driven by the photospheric vortices. The transfer of energy from photospheric vortices to Alfvén waves and chromospheric transverse waves has been demonstrated in numerical simulations of the lower solar atmosphere (e.g., Fedun et al., 2011b).

The measured wave properties also reveal interesting information about the chromospheric waves. In particular, the measured velocity amplitudes (Fig. 6) suggest that waves with periods in the range 50 – 500 s have similar power. However, the results presented here are restricted to incompressible waves confined in one particular structure in the chromosphere. A more in depth study taking into account numerous chromospheric structures

is required before more definite conclusions on this issue can be drawn.

Finally, we highlight here that our results have some limitations. The limitations are related to the inability to resolve small amplitude ($\lesssim 25$ km) transverse waves due to spatial resolution. The demonstrated relationship between displacement amplitude and period (Fig. 5) implies that spatial resolution also limits the ability to detect short period waves ($\lesssim 30$ s). On the other end of the scale, the known lifetimes of the chromospheric structures (i.e., 3 – 5 minutes) also limits the observations of longer period waves (> 200 s). This is reflected in the low number of observations of wave with longer periods. Some of these limitations may be overcome if more advanced techniques are employed for wave tracking, e.g., calculating sub-pixel displacements could reveal smaller amplitude wave phenomena.

The authors would like to thank D. B. Jess, M. Mathioudakis and A. Hillier for a number of helpful discussions. Observations were obtained at the National Solar Observatory, operated by the Association of Universities for Research in Astronomy, Inc. (AURA) under agreement with the National Science Foundation. We thank the technical staff at DST for their help and support during the observations. This work is supported by the UK Science and Technology Facilities Council (STFC). RM is grateful to Northumbria University for the award of an Anniversary Fellowship and to the Royal Astronomical Society (RAS) for the award of an RAS travel grant. GV grateful to the Leverhulme Trust for the award of a fellowship. SS research is supported by the Australian Research Council Future Fellowship. RE acknowledges M. Kéray for patient encouragement and is also grateful to NSF, Hungary (OTKA, Ref. No. K83133).

REFERENCES

- Andries, J., Arregui, I., & Goossens, M. 2005, *ApJ*, 624, L57
 Antolin, P. & Shibata, K. 2010, *ApJ*, 712, 494
 Antolin, P. & Verwichte, E. 2011, *ApJ*, 736, 121
 Aschwanden, M. J. 2005, *Physics of the Solar Corona. An Introduction with Problems and Solutions* (2nd edition) (Pour la Science)
 Balmaceda, L., Vargas Domínguez, S., Palacios, J., Cabello, I., & Domingo, V. 2010, *A&A*, 513, L6
 Banerjee, D., Erdélyi, R., Oliver, R., & O’Shea, E. 2007, *Sol. Phys.*, 246, 3
 Berger, T. E., Loefeldahl, M. G., Shine, R. S., & Title, A. M. 1998, *ApJ*, 495, 973
 Berger, T. E., Schrijver, C. J., Shine, R. A., et al. 1995, *ApJ*, 454, 531
 Berger, T. E. & Title, A. M. 2001, *ApJ*, 553, 449
 Bonet, J. A., Márquez, I., Sánchez Almeida, J., Cabello, I., & Domingo, V. 2008, *Astrophysical Journal Letters*, 687, L131
 Brandt, P. N., Scharmer, G. B., Ferguson, S., Shine, R. A., & Tarbell, T. D. 1988, *Nature*, 335, 238
 Carlsson, M., Stein, R. F., Nordlund, Å., & Scharmer, G. B. 2004, *ApJ*, 610, L137
 Cauzzi, G., Reardon, K. P., Uitenbroek, H., et al. 2008, *A&A*, 480, 515
 Chitta, L. P., van Ballegoijen, A. A., Rouppe van der Voort, L., DeLuca, E. E., & Kariyappa, R. 2012, *ApJ*, 752, 48
 Cranmer, S. R. & van Ballegoijen, A. A. 2005, *ApJS*, 156, 265
 Cranmer, S. R., van Ballegoijen, A. A., & Edgar, R. J. 2007, *ApJS*, 171, 520
 De Moortel, I. & Nakariakov, V. M. 2012, *Royal Society of London Philosophical Transactions Series A*, 370, 3193
 De Pontieu, B., McIntosh, S. W., Carlsson, M., et al. 2007, *Science*, 318, 1574
 Domínguez Cerdeña, I., Kneer, F., & Sánchez Almeida, J. 2003, *ApJ*, 582, L55
 Dowdy, Jr., J. F., Rabin, D., & Moore, R. L. 1986, *Sol. Phys.*, 105, 35
 Dymova, M. V. & Ruderman, M. S. 2005, *Sol. Phys.*, 229, 79
 Dymova, M. V. & Ruderman, M. S. 2006, *A&A*, 459, 241
 Edwin, P. M. & Roberts, B. 1982, *Sol. Phys.*, 76, 239
 Edwin, P. M. & Roberts, B. 1983, *Sol. Phys.*, 88, 179
 Erdélyi, R. 2006, *Royal Society of London Philosophical Transactions Series A*, 364, 351
 Erdélyi, R. & Fedun, V. 2007, *Science*, 318, 1572
 Erdélyi, R. & Fedun, V. 2010, *Sol. Phys.*, 263, 63
 Erdélyi, R. & Morton, R. J. 2009, *A&A*, 494, 295
 Erdélyi, R. & Taroyan, Y. 2008, *A&A*, 489, L49
 Faurobert, M., Arnaud, J., Vigneau, J., & Frisch, H. 2001, *A&A*, 378, 627
 Fedun, V., Shelyag, S., & Erdélyi, R. 2011a, *ApJ*, 727, 17
 Fedun, V., Shelyag, S., Verth, G., Mathioudakis, M., & Erdélyi, R. 2011b, *Annales Geophysicae*, 29, 1029
 Fedun, V., Verth, G., Jess, D. B., & Erdélyi, R. 2011c, *ApJ*, 740, L46
 Goossens, M., Andries, J., & Aschwanden, M. J. 2002, *A&A*, 394, L39
 Goossens, M., Terradas, J., Andries, J., Arregui, I., & Ballester, J. L. 2009, *A&A*, 503, 213
 He, J., Marsch, E., Tu, C., & Tian, H. 2009a, *ApJ*, 705, L217
 He, J.-S., Tu, C.-Y., Marsch, E., et al. 2009b, *A&A*, 497, 525
 Ionson, J. A. 1978, *ApJ*, 226, 659

- Ishikawa, R., Tsuneta, S., Kitakoshi, Y., et al. 2007, *A&A*, 472, 911
- Jess, D. B., Mathioudakis, M., Christian, D. J., et al. 2010, *Sol. Phys.*, 261, 363
- Jess, D. B., Mathioudakis, M., Erdélyi, R., et al. 2009, *Science*, 323, 1582
- Jess, D. B., McAteer, R. T. J., Mathioudakis, M., et al. 2007, *A&A*, 476, 971
- Jess, D. B., Pascoe, D. J., Christian, D. J., et al. 2012a, *ApJ*, 744, L5
- Jess, D. B., Shelyag, S., Mathioudakis, M., et al. 2012b, *ApJ*, 746, 183
- Keys, P. H., Mathioudakis, M., Jess, D. B., et al. 2011, *ApJ*, 740, L40
- Kitiashvili, I. N., Kosovichev, A. G., Mansour, N. N., Lele, S. K., & Wray, A. A. 2012, *Phys. Scr.*, 86, 018403
- Kitiashvili, I. N., Kosovichev, A. G., Mansour, N. N., & Wray, A. A. 2011, *ApJ*, 727, L50
- Klimchuk, J. A. 2006, *Sol. Phys.*, 234, 41
- Kuridze, D., Morton, R. J., Erdélyi, R., et al. 2012, *ApJ*, 750, 51
- Leenaarts, J., Carlsson, M., & Rouppe van der Voort, L. 2012, *ApJ*, 749, 136
- Leenaarts, J., Rutten, R. J., Carlsson, M., & Uitenbroek, H. 2006, *A&A*, 452, L15
- Luna, M., Terradas, J., Oliver, R., & Ballester, J. L. 2010, *ApJ*, 716, 1371
- Markwardt, C. B. 2009, in *ASPSCS*, Vol. 411, *Astronomical Data Analysis Software and Systems XVIII*, ed. D. A. Bohlender, D. Durand, & P. Dowler, 251
- Matsumoto, T. & Kitai, R. 2010, *ApJ*, 716, L19
- Matsumoto, T. & Shibata, K. 2010, *ApJ*, 710, 1857
- Matthaeus, W. H., Zank, G. P., Oughton, S., Mullan, D. J., & Dmitruk, P. 1999, *ApJ*, 523, L93
- McKenzie, J. F., Axford, W. I., & Banaszekiewicz, M. 1997, *Geophys. Res. Lett.*, 24, 2877
- Moll, R., Cameron, R. H., & Schüssler, M. 2011, *A&A*, 533, A126
- Moll, R., Cameron, R. H., & Schüssler, M. 2012, *A&A*, 541, A68
- Morton, R. & Erdélyi, R. 2009, *A&A*, 605, 493
- Morton, R. J., Verth, G., Jess, D. B., et al. 2012, *Nat. Commun.*, 3, 1325
- November, L. J. & Simon, G. W. 1988, *ApJ*, 333, 427
- Okamoto, T. J. & De Pontieu, B. 2011, *ApJ*, 736, L24
- Orozco Suárez, D. & Bellot Rubio, L. R. 2012, *ApJ*, 751, 2
- Pascoe, D. J., Wright, A. N., & De Moortel, I. 2011, *ApJ*, 731, 73
- Peter, H. 2001, *A&A*, 374, 1108
- Pietarila, A., Hirzberger, J., Zakharov, V., et al. 2009, *A&A*, 502, 647
- Reardon, K. P., Uitenbroek, H., & Cauzzi, G. 2009, *A&A*, 500, 1239
- Rimmele, T. R. 2004, in *Society of Photo-Optical Instrumentation Engineers (SPIE) Conference Series*, Vol. 5490, *Society of Photo-Optical Instrumentation Engineers (SPIE) Conference Series*, ed. D. Bonaccini Calia, B. L. Ellerbroek, & R. Ragazzoni, 34–46
- Robertson, D., Ruderman, M. S., & Taroyan, Y. 2010, *A&A*, 515, A33
- Ruderman, M. S. & Roberts, B. 2002, *ApJ*, 577, 475
- Ruderman, M. S., Verth, G., & Erdélyi, R. 2008, *ApJ*, 686, 694
- Rutten, R. J. 2006, in *Astronomical Society of the Pacific Conference Series*, Vol. 354, *Solar MHD Theory and Observations: A High Spatial Resolution Perspective*, ed. J. Leibacher, R. F. Stein, & H. Uitenbroek, 276
- Rutten, R. J. 2007, in *Astronomical Society of the Pacific Conference Series*, Vol. 368, *The Physics of Chromospheric Plasmas*, ed. P. Heinzel, I. Dorotović, & R. J. Rutten, 27
- Sánchez Almeida, J., Márquez, I., Bonet, J. A., Domínguez Cerdeña, I., & Müller, R. 2004, *ApJ*, 609, L91
- Schrijver, C. J. & Title, A. M. 2003, *ApJ*, 597, L165
- Schuck, P. W. 2006, *ApJ*, 646, 1358
- Shelyag, S., Fedun, V., Erdélyi, R., Keenan, F. P., & Mathioudakis, M. 2012a, in *ASPSCS*, Vol. 463, *ASPSCS*, ed. T. R. Rimmele, A. Tritschler, & F. e. a. Wöger, 107
- Shelyag, S., Fedun, V., Keenan, F. P., Erdélyi, R., & Mathioudakis, M. 2011a, *Annales Geophysicae*, 29, 883
- Shelyag, S., Keys, P., Mathioudakis, M., & Keenan, F. P. 2011b, *A&A*, 526, A5
- Shelyag, S., Mathioudakis, M., & Keenan, F. P. 2012b, *ApJ*, 753, L22
- Soler, R., Oliver, R., & Ballester, J. L. 2009a, *ApJ*, 699, 1553
- Soler, R., Oliver, R., & Ballester, J. L. 2009b, *ApJ*, 707, 662
- Spruit, H. C. 1982, *Sol. Phys.*, 75, 3
- Starck, J.-L. & Murtagh, F. 2002, *Astronomical image and data analysis* (Berlin: Springer)
- Stein, R. F. & Nordlund, A. 1998, *ApJ*, 449, 914
- Terradas, J., Goossens, M., & Verth, G. 2010, *A&A*, 524, A23
- Terradas, J., Oliver, R., & Ballester, J. L. 2006, *ApJ*, 642, 533
- Title, A. M., Tarbell, T. D., Topka, K. P., et al. 1989, *ApJ*, 336, 475
- Tomczyk, S., McIntosh, S. W., Keil, S. L., et al. 2007, *Science*, 317, 1192
- Tu, C.-Y. & Marsch, E. 1995, *Space Sci. Rev.*, 73, 1
- van Ballegoijen, A. A., Asgari-Targhi, M., Cranmer, S. R., & DeLuca, E. E. 2011, *ApJ*, 736, 3
- Van Doorselaere, T., Debosscher, A., Andries, J., & Poedts, S. 2004, *A&A*, 424, 1065
- Vargas Domínguez, S., Palacios, J., Balmaceda, L., Cabello, I., & Domingo, V. 2011, *MNRAS*, 416, 148
- Vecchio, A., Cauzzi, G., Reardon, K. P., Janssen, K., & Rimmele, T. 2007, *A&A*, 461, L1
- Verth, G. & Erdélyi, R. 2008, *A&A*, 486, 1015
- Vigeesh, G., Fedun, V., Hasan, S. S., & Erdélyi, R. 2012, *ApJ*, 755, 18
- Vögler, A., Shelyag, S., Schüssler, M., et al. 2005, *A&A*, 429, 335
- Wang, T. 2011, *Space Sci. Rev.*, 16
- Wedemeyer-Böhm, S., Lagg, A., & Nordlund, Å. 2009, *Space Sci. Rev.*, 144, 317
- Wedemeyer-Böhm, S. & Rouppe van der Voort, L. 2009, *A&A*, 507, L9
- Wedemeyer-Böhm, S., Scullion, E., Steiner, O., et al. 2012, *Nature*, 486, 505
- Wöger, F., von der Lühe, O., & Reardon, K. 2008, *A&A*, 488, 375
- Zaqarashvili, T. V. & Erdélyi, R. 2009, *Space Sci. Rev.*, 149, 355
- Zaqarashvili, T. V., Khodachenko, M. L., & Rucker, H. O. 2011, *A&A*, 529, A82